nature photonics

Article

https://doi.org/10.1038/s41566-025-01719-9

Integrated electro-optic digital-to-analogue link for efficient computing and arbitrary waveform generation

Received: 11 December 2024

Accepted: 10 June 2025

A list of authors and their affiliations appears at the end of the paper

The rapid growth in artificial intelligence and modern communication systems demands innovative solutions for increased computational power and advanced signalling capabilities. Integrated photonics, leveraging the analogue nature of electromagnetic waves at the chip scale, offers a promising complement to approaches based on digital electronics. To fully unlock their potential as analogue processors, establishing a common technological base between conventional digital electronics and analogue photonics is imperative for building next-generation computing and communications systems. However, the absence of an efficient interface has thus far critically challenged a comprehensive demonstration of the advantages of analogue photonic hardware, with the scalability, speed and energy consumption as primary bottlenecks. Here we address this challenge and demonstrate a general electro-optic digital-to-analogue link enabled using foundry-based lithium niobate nanophotonics. Using purely digital electronic inputs, we achieve the on-demand generation of both analogue optical and electronic waveforms at information rates of up to 186 Gb s^{-1}. The optical waveforms address the digital-to-analogue electro-optic conversion challenge in photonic computing, showcasing high-fidelity Modified National Institute of Standards and Technology image encoding with an ultralow power consumption of 0.058 pJ b^{-1}. The electronic waveforms enable a pulse-shaping-free microwave arbitrary waveform generation method with ultrabroadband tunable delay and gain. Our results pave the way for efficient and compact digital-to-analogue conversion paradigms enabled by integrated photonics, and underscore the transformative impact that analogue photonic hardware may have on various applications, such as computing, optical interconnects and high-speed ranging.

The development of efficient, high-bandwidth communication systems and novel computational paradigms has been driven by advancements in high-performance computing and complex signal-processing infrastructure, leading to substantial scientific and industrial impact[1,2]. Examples include tensor processing units[3], neuromorphic chips[4] and high-frequency electronics[5,6], which crucially satisfy the most stringent demands for increased computing power and data transmission rates. In recent years, there has also been a burgeoning interest in the development of analogue hardware to handle exponential growth in data volumes and generate ultrabroadband electronic waveforms[7]. Photonics is ideally suited to these tasks as it offers higher capacity and throughput than incumbent electronic approaches while also consuming substantially less energy[8–16]. Moreover, photonic integration supports compact form factors, offers excellent scalability and enables cost-effective production.

For photonic technologies to be seamlessly integrated into computing and communication systems, a high-speed, energy-efficient

e-mail: ysong1@g.harvard.edu; yaowenhu@pku.edu.cn; loncar@seas.harvard.edu

interface between the digital electronic domain (used for information storage) and the analogue photonics domain (used for information processing) is essential. Currently, this interface is primarily established via a two-step process: digital-to-analogue converters (DACs) are used to convert binary words into analogue electrical signals, which are then used to drive electro-optic (EO) modulators. However, there is a substantial system complexity and cost associated with the high-speed DAC circuits that are needed to drive state-of-the-art EO modulators to their analogue bandwidth limits that exceed 100 GHz (refs. 17,18). To address this bottleneck, previous efforts have utilized silicon photonics to integrate DACs and EO modulators for higher-order-modulation-format optical communications[19–25]. However, the silicon platform and its plasma-dispersion-based EO conversion are associated with large insertion losses, bandwidth limitations and high reverse-bias/alternating-current-driving voltages, which constrained these demonstrations to only two-bit resolution and a prohibitive level of performance efficiency. A general and scalable digital-to-analogue link that meets the critical requirements for high-performance, large-scale analogue photonic computing and signalling remains elusive.

In this Article we overcome the above mentioned challenges by utilizing thin-film lithium niobate (TFLN) photonics to demonstrate an electro-optic digital-to-analogue link (EO-DiAL) device, based on a multi-electrode Mach–Zehnder interferometer (MZI) design. The device can realize high-speed, multi-level optical encoding using two-level electrical drives, fully leveraging both efficient electro-optical interaction[26–28] and low optical and microwave loss properties[29,30] of the TFLN platform. The EO-DiAL device acts as an alternative to conventional electronic DAC and EO modulator pairs, with the potential to become a key component in next-generation photonic computing architectures which rely heavily on EO conversion[31]. Furthermore, the device expands the microwave photonic signal-generation toolset by offering a novel radiofrequency arbitrary waveform generation (RF-AWG) method. Considering these application spaces, we demonstrate that the EO-DiAL produces a data stream in the optical domain with four-bit amplitude resolution and 21.505 ps temporal resolution when it is driven by four-bit binary words, leading to an effective data rate of 186 Gb s^{-1} and an energy consumption of 0.058 pJ b^{-1}. To illustrate the potential of this platform for computing, we encode down-sampled Modified National Institute of Standards and Technology (MNIST) handwritten digits onto an optical carrier with high fidelity. We then combine the EO-DiAL optical output with fast photodetection to perform optical-to-electronic (OE) conversion, thus realizing electronic RF-AWG. In contrast to conventional microwave photonic methods for AWG, such as optical pulse shaping[32–35], our approach is based on continuous-wave (CW) light inputs, does not require optical fanout or resonant filters and is facilitated by coherent phase control in the EO-DiAL. Hence, the synthesized arbitrary waveforms exhibit no signal downtime, and they are compatible with RF-over-fibre link technologies[36], among which we show tunable RF delay and measurements towards broadband power gain in the generated waveforms.

Results

EO-DiAL concept

The EO-DiAL concept generalized to N bits of resolution, using a segmented MZI structure with travelling-wave electrodes on a chip, is illustrated in Fig. 1a. An N-bit EO-DiAL features N pairs of push–pull electrode segments, instead of the conventional single pair. Each pair is twice as long as the next and thus requires a twofold smaller voltage (V_π) to change the phase of the propagating light by π (180°). In other words, if the longest segment is characterized by the switching voltage V_π, then the second longest segment is characterized by $2V_\pi$ and the shortest segment by $2^{N-1}V_\pi$. A stream of N-bit words (to be optically encoded) is represented by N binary voltage signals. Words are encoded sequentially in time t, each represented by a set of $V_n(t = mT)$. Here, n is the segment number (with $n = 0$ representing the shortest segment with electrode length L, corresponding to the least significant bit, and $n = N - 1$ representing the longest segment with electrode length of $2^{N-1}L$, corresponding to the most significant bit), $1/T$ is the bit rate and m is an integer index for sequential words. The $V_n(t)$ voltage sequences each assume either of the two values (V_{high}, V_{low}). When all segments are driven together by a set of $V_n(t)$, the optical fields in the push and pull arms accumulate a phase difference $\Delta\phi$ given by:

$$\Delta\phi(t) = \frac{\pi}{2^{N-1}V_\pi}\left(\sum_{n=0}^{N-1} V_n(t)2^n\right). \tag{1}$$

The power transfer function of the EO-DiAL is given by $T = \frac{1}{2}\left(1+\sin\left(\Delta\phi(t)\right)\right)$, which is proportional to $\Delta\phi(t)$ in the limit of small $\Delta\phi(t)$ (satisfied when $|V_n| \ll V_\pi$) and when the MZI is biased at quadrature. As purely digital modulations partition the total $\Delta\phi(t)$ into 2^N levels (the quantity of equation (1) in parentheses), the EO-DiAL output power is N-bit-resolved and both EO conversion and digital-to-analogue conversion is achieved simultaneously, without an external electronic DAC. The four-bit implementation considered here and its corresponding bit-wise addressable optical transmission is explicitly presented in Fig. 1b.

TFLN implementation

The EO-DiAL device, shown in Fig. 2a, occupies a compact footprint of only 30.73 mm^2 and is fabricated using a mature wafer-scale TFLN process at a commercial semiconductor foundry (a multi-project wafer run offered by HyperLight Corporation). The main components of the device are shown in Fig. 2b and include electrode pads, capacitance-loaded coplanar lines, 50 Ω terminations, metal routing, low-loss fibre-to-chip grating couplers and heaters (see Supplementary Information for details about these and other components). In particular, four push–pull electrode segments (Fig. 2c S0–S3, with electrode lengths of 0.25, 0.50, 1.00 and 2.00 cm, respectively) form an MZI, mapping to four bits of resolution. Note that the low-optical-loss and wide-EO-bandwidth characteristics of TFLN modulators ensure the fast and low energy consumption of the EO-DiAL (see Supplementary Information for optical loss characterization). To operate the EO-DiAL at a high bandwidth, the frequency-dependent V_π values for the electrode segments must satisfy the factor-of-two relationship throughout the complete frequency content of the digital modulation patterns. This translates to a flat frequency-response requirement for each segment, justifying the need for capacitance-loaded RF transmission lines which alleviate V_π–bandwidth trade-offs induced by microwave losses[37]. The measured V_π values for segments S0–S3 are 10.19, 5.97, 3.27 and 1.69 V, respectively (Fig. 2d). To account for residual deviations from the target V_π relationship, probably due to fabrication imperfections, the amplitudes of $V_n(t)$, defined as $|V_n|$, are slightly tuned to enforce linearity between $|V_n|/V_\pi$ and segment length L_n (Fig. 2e), resulting in $|V_n|$ values of 200, 195, 210 and 215 mV, respectively. This set of $|V_n|$ is characteristic of the device and is fixed throughout the experiments. Without these imperfections, $|V_n|$ should be identical for all n. Normalized S parameters (Fig. 2f) for segments S0–S2 indicate a low electrical–electrical (EE) return loss and a near-flat EO response up to a modulation frequency of 50 GHz (limited by the bandwidth of our measurement equipment). On the other hand, segment S3 has an EO 3 dB cut-off of about 30 GHz and a simulated 5 dB cut-off of about 100 GHz, which, although sufficient for this work, may be improved in future iterations. We note that these EO properties and the EO-DiAL design targets reported here are consistently reproduced across devices on all dies measured (seven dies total, see Supplementary Figs. 1–3), underscoring the high yield and scalability of complex TFLN photonic circuits. Finally, the linearity of the EO-DiAL device is examined by synchronizing four binary modulation sequences (each sampled at 46.5 Gb s^{-1}) that, when combined, probe each level of the device's

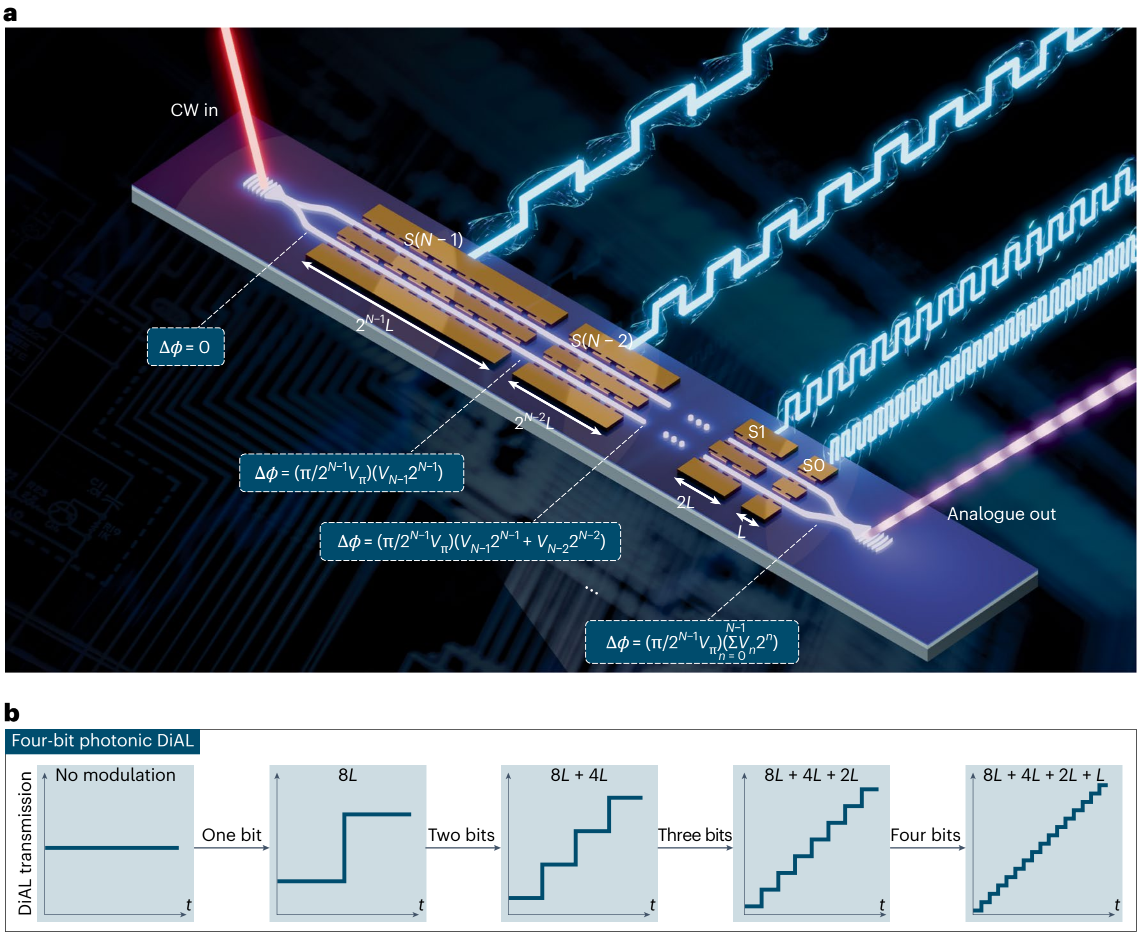

Fig. 1 | Photonic-integrated EO-DiAL concept. a, Illustration of an *N*-bit-resolution EO-DiAL architecture. Key components include an MZI that features *N* modulation segments with lengths (and hence V_π values) related by factors of two. The shortest (longest) segment controls the least (most) significant bit of the *N*-bit analogue value (see equation (1) and derivation in the Supplementary Information). The *n*th bit is set by a digital electronic input $V_n \in \{V_{\text{high}}, V_{\text{low}}\}$ applied to the *n*th segment with length 2^nL. Segments are labelled by the bit they address: the least significant bit (bit 0) corresponds to the shortest segment and is labelled S0; the most significant bit (bit $N-1$) corresponds to the longest segment and is labelled S($N-1$). The insets in dashed boxes mark the phase accumulation $\Delta\phi$ after each segment, from the longest to the shortest segment. As $\Delta\phi$ is bit-wise-addressable, so is the MZI transmission, when operating near the quadrature point. Thus, a fast switching sequence of $V_n(t)$ amounts to a continuously and rapidly updating *N*-bit-resolved analogue data stream output by the DiAL device. Notably, digital-to-analogue conversion occurs directly from the electronic to the optical domain, without the overhead of electronic DACs. **b**, Illustration of the four-bit-resolved transmission of the EO-DiAL implemented on TFLN, in this work.

four bits of amplitude resolution. The amplitudes conform well to a linear fit, suggesting a high degree of linearity (Fig. 2g).

Efficient EO digital-to-analogue interface

To benchmark the performance of the EO-DiAL device for efficient EO conversion within photonic computing architectures (Fig. 3a), two key performance metrics were systematically evaluated, namely, the maximal encoding speed and the minimal energy requirement for high-fidelity encoding. First, sets of four binary modulation sequences clocked at an aggregate data rate of 124 Gb s^{-1} and 186 Gb s^{-1} are delivered to modulation segments S0–S3 of the EO-DiAL. Each sequence consists of 500 random bits that altogether combine into one sequence of 500 random four-bit words. The four-bit-resolved amplitude is directly observed using a real-time oscilloscope to evaluate the encoding quality. However, in real computing applications, this encoded light would be routed into a photonic processor. As shown in Fig. 3b, the optical amplitude closely follows the ideal random data sequence at both data rates. Thus, the electronic data, presented in binary form, are successfully encoded onto the optical carrier. We note that imperfections at 186 Gb s^{-1} manifest as reduced amplitude swing and perceivable rise and drop times between words, as shown by the expanded traces in Fig. 3b. At this higher data rate, deviations from perfect encoding are attributed to operating near the bandwidth limit of both the driving electronic circuit (digital driver and RF cables) and the photonic circuit (limited by segment S3). Indeed, the consequence of a finite bandwidth on encoding practical data is shown in Fig. 3c. Here, a down-sampled 28 × 28 MNIST image, represented by a sequence of 784 four-bit words, is converted into the optical domain at a rate of 186 Gb s^{-1} while consuming 0.104 pJ b^{-1}. The primary features of the digit are accurately preserved, although a weak shadowing effect is observed. As the EO-DiAL operates as a DAC-free EO converter, we next explore the potential for machine learning algorithms to process these images. We apply a classification model on both computer-encoded and EO-DiAL-encoded test images. This provides insight into the potential performance of photonic computing systems that are implementing the model. We define the encoding accuracy of the EO-DiAL according to the overlap (represented by a confusion matrix) between both classification sets (Fig. 3d), and we find that 95% of 100 MNIST images are accurately encoded in the optical domain. Finally, the energy consumption of digital-to-analogue and EO conversion is explored at the higher encoding rate (186 Gb s^{-1}) in relation to the encoding fidelity. In Fig. 3e, reconstructed images at three different optical powers (that is, detected

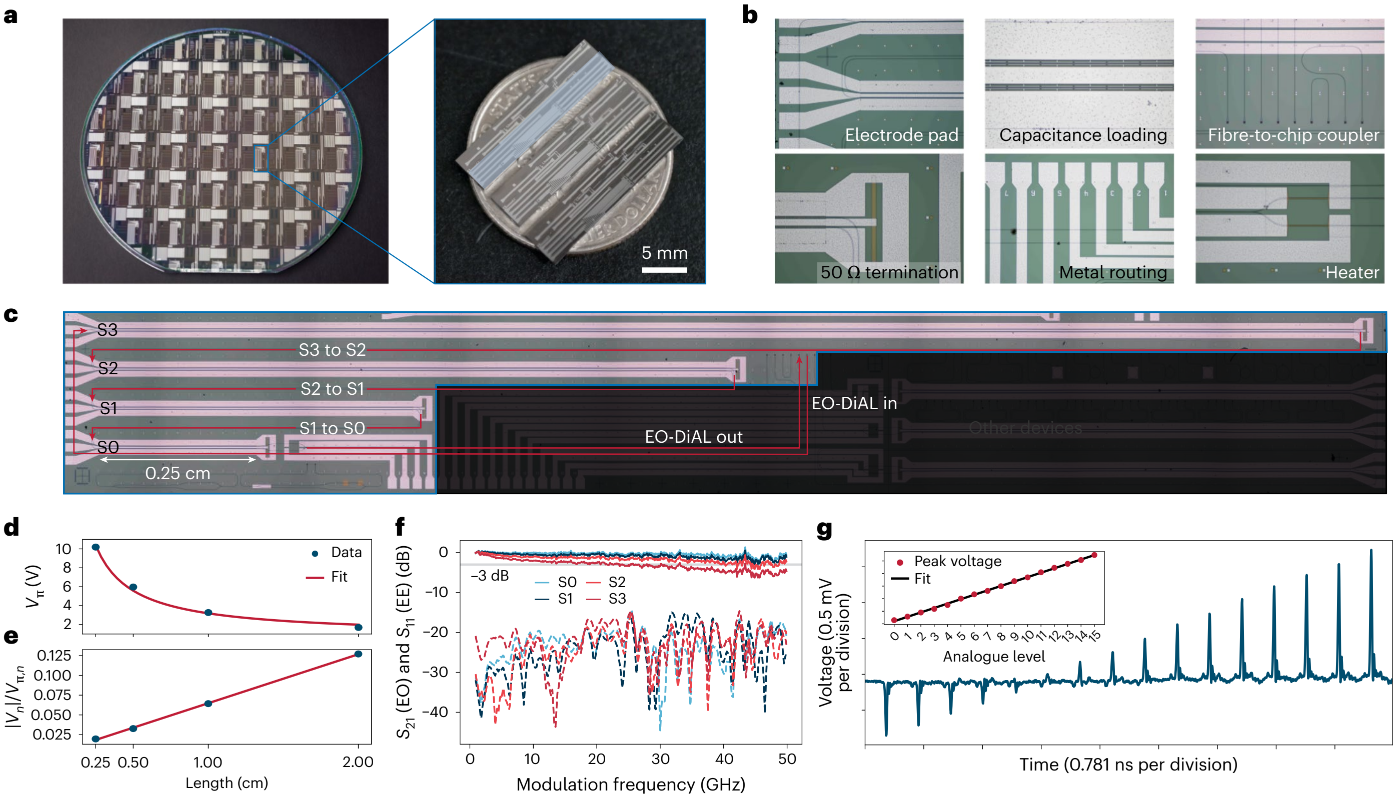

Fig. 2 | EO-DiAL implementation and device characterization. **a**, Wafer-scale process (left) used for the EO-DiAL devices (right) in this work. **b**, Individual components comprising the EO-DiAL device, including electrode pads, capacitance-loaded RF transmission lines, fibre-to-chip grating couplers, 50 Ω terminators, metal routing and heaters (see Supplementary Information for details). **c**, Optical microscope image of the EO-DiAL architecture implemented with TFLN nanophotonics, consisting of four modulation segments (S0–S3) with lengths 0.25, 0.50, 1.00 and 2.00 cm, respectively. The optical signal path is traced by the dark red arrows. **d**, Measured V_π for each modulation segment. **e**, Ratio of $|V_n|/V_{\pi,n}$, for $|V_n|$ used to calibrate out deviations from the factor-of-two V_π relationship due to fabrication imperfections. **f**, EO forward transmission (EO S_{21}) and electric–electric input reflection (EE S_{11}) for each modulation segment. Segment S3 achieves an EO 3 dB bandwidth of 30 GHz, whereas nearly flat frequency responses of up to 50 GHz are maintained for segments S0–S2. The EE return loss is low for all segments. **g**, Linear optical intensity relation across all 16 levels encoded within the dynamic range of the four-bit EO-DiAL (21.505 ps per level). The inset shows a linear fit of optical intensity versus analogue level (0–15, or four bits of information).

optical power values of −17.5, −11.6 and −5.6 dBm) and two different electrical powers (applied driving voltages $|V_n| = 100$ and 200 mV) indicate increases in the overall signal-to-noise ratio and dynamic range when more power is consumed. The driving voltage of $|V_n| \approx 200$ mV is sufficient to reach at least 95% encoding accuracy across all optical power levels considered. On the other hand, $|V_n| \approx 100$ mV with −17.5 dBm of detected optical power can still achieve an encoding accuracy of 89%, while expending a total of 0.058 pJ b^{-1} (Fig. 3f).

Radiofrequency arbitrary waveform generation and manipulation

A schematic of the EO-DiAL configured for RF-AWG is shown in Fig. 4a. Here, CW light is shaped by four digitally modulated segments S0–S3 such that an RF arbitrary waveform with four-bit amplitude resolution is imprinted onto the optical carrier and subsequently undergoes OE conversion via fast photodetection. First, to demonstrate basic RF-AWG functionality, six standard waveforms (sine, trapezoid, sinc, chirp, square and ramp) were separately synthesized (Fig. 4b). Next, identical random arbitrary waveforms, each with distinctly resolved features every $T = 21.505$ ps, were produced at eleven instances precisely 21.505 ps apart by fine-tuning the optical delay using a motorized delay line. Matching modulation patterns in the detected waveforms show the accurate word-by-word delay (Fig. 4c). Similarly, a sinc pulse was stored with high fidelity and low loss in an optical fibre, and released 480 ns later (Fig. 4d). The optical path length thus endows our EO-DiAL-based RF-AWG with additional functionalities, such as picosecond precision, broadband RF delay and long-timescale RF signal storage and release. These functionalities are reminiscent of skew control between the channels of an electronic RF arbitrary waveform generator and synchronization between multiple units within an electronic RF-AWG network, which nominally require additional complex circuitry.

Next, the broadband OE gain transfer of the RF-AWG is measured through the electronic-to-optical-to-electronic system response (Fig. 4e). A net positive gain up to 35 GHz can be achieved, after applying 11.6 dB of optical gain to amplify the EO-DiAL output supplied by an erbium-doped fibre preamplifier, in conjunction with transimpedance gain. This S_{21} response of the system has an identical shape to the transimpedance amplifier response, indicating flat optical-to-RF gain transfer. The 0 dB level is referenced to the summed vector network analyzer source power to drive segments S0–S3 (−6.0 dBm total, as described in the Supplementary Information). Note that this response represents a digital-to-analogue response, in contrast to conventional RF-over-fibre link gain where the modulation and demodulated waveforms are identical. Finally, using a fast photodiode with a high saturation power, the incident average optical power is varied from 1 to 15.9 mW, and the RF power generated by output triangular waves (Fig. 4f inset) are estimated from the root-mean-squared voltage produced across a load of 50 Ω. Note that, in this approach, the broadband electronic gain on the synthesized waveform is inherited from the optical gain alone. Thus, broadband microwave gain can be achieved in a straightforward manner by leveraging the optical

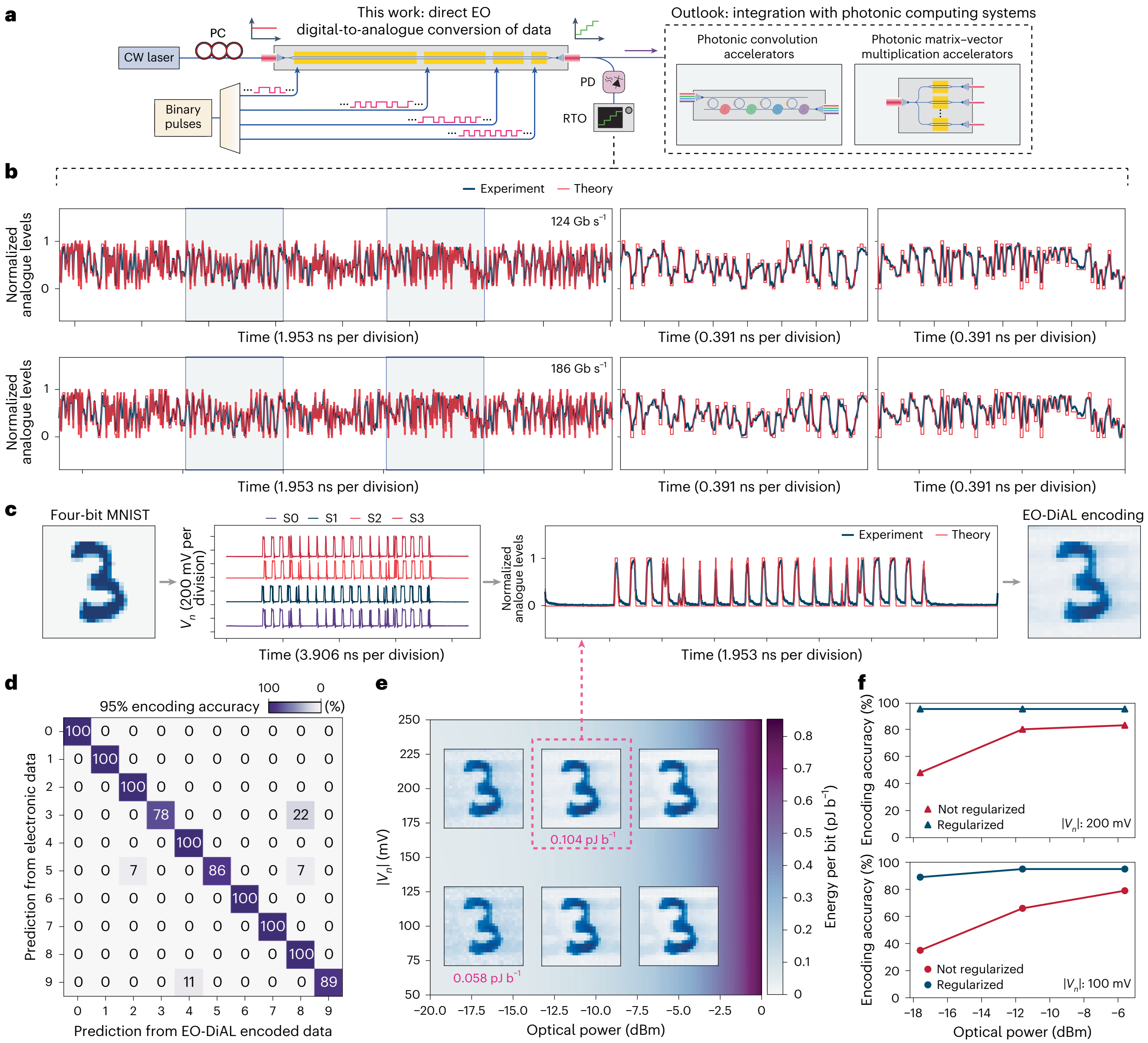

Fig. 3 | High-speed and energy-efficient EO conversion of data. a, Schematic of the EO-DiAL operated as an EO DAC in photonic computing systems. PC, polarization controller; PD, photodetector; RTO, real-time oscilloscope. **b**, A random sequence of 500 four-bit words encoded by the device at effective data rates of 124 Gb s^{-1} (top) and 186 Gb s^{-1} (bottom), which correspond to independent modulation rates of 31 Gb s^{-1} and 46.5 Gb s^{-1} per electrode segment, respectively. The two right-hand panels for each sequence are expansions of the start and end of the traces (shaded in blue). **c**, Left to right: down-sampled MNIST image (28 × 28 pixels) to be flattened into four-bit pixel arrays of size 784; binary modulation patterns applied to segments S0–S3; EO conversion and digital-to-analogue conversion by the device at 186 Gb s^{-1} and 0.104 pJ b^{-1}; and reconstructed MNIST image from the photodetected optical intensities. The weak shadowing effect in this reconstructed image is due to the bandwidth limits in the system, corresponding to finite rise and drop times. **d**, Normalized confusion matrix that compares the classification outcomes between applying a machine learning model on test sets consisting of (1) original MNIST images (defined as ground truth) and (2) EO-DiAL-encoded MNIST images, using experimental parameters identical to **c**. Ninety-five per cent of EO-DiAL-encoded images faithfully reproduce the fully electronic inferences and thus are considered to be accurately encoded. Supplementary Fig. 5 shows normalized confusion matrices for other combinations of optical and electrical parameters. **e**,**f**, Encoding quality (**e**) and encoding accuracy (**f**) as a function of the electronic and optical energy consumption. In **e**, the background colour gradient includes both optical and electrical energy consumption, and microheater dissipation when thermally biasing the MZI at quadrature. With 100 mV for each $|V_n|$ and −17.5 dBm optical power incident on the detector, which amounts to 0.058 pJ b^{-1}, 89% of the images are accurately encoded.

domain, in contrast to electronically amplifying electrical DAC outputs which have electronic bandwidth limitations. As shown in Fig. 4f, an RF power of up to 0.16 mW is generated, which is yet to surpass the total digital modulation power. Nevertheless, agreement between the measurement and an expected quadratic relation, between the optical power incident on the photodiode and the generated RF power, indicates linear OE conversion by the photodiode. This indicates that a lower V_π and a higher photodiode saturation mean that an above 0 dB digital-to-analogue gain is within reach (see Supplementary Information for a detailed discussion).

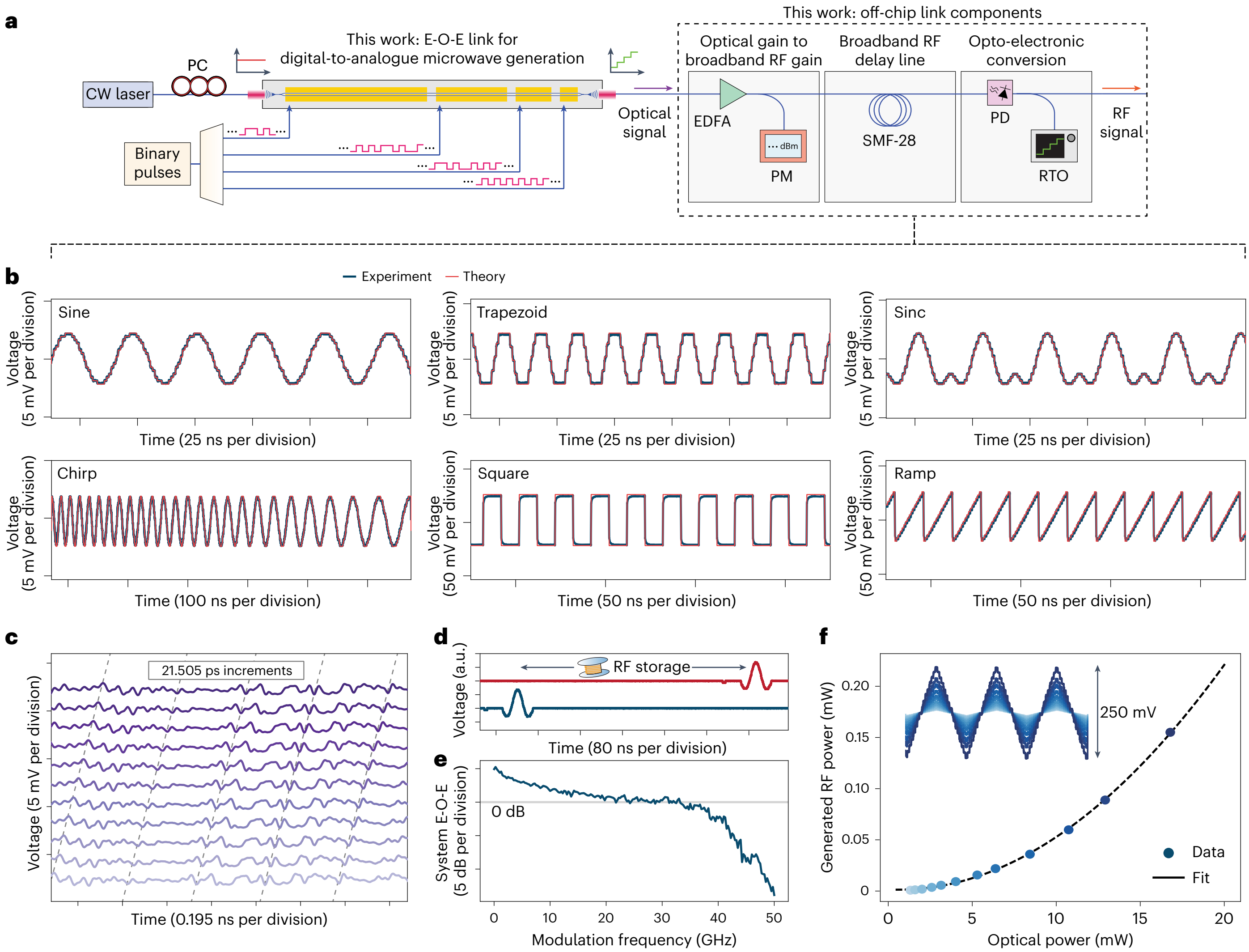

Fig. 4 | Microwave photonic RF-AWG. a, Schematic of the EO-DiAL operated for microwave photonic RF-AWG based on a CW optical input. Optical gain and optical delays are subsequently applied for the broadband optical–microwave gain transfer, delay, storage and release of the RF arbitrary waveform. EDFA, erbium-doped fibre amplifier; E-O-E, electronic-to-optical-to-electronic; PM, powermeter; SMF, single-mode fibre. **b**, Standard waveforms encoded by the EO-DiAL onto the optical carrier and then converted into the electronic domain using a fast photodetector. **c**,**d**, Tuning of the optical path length (in this case, incremental delays of ~21.505 ps) before demodulation enables the broadband, word-by-word delay of a random RF waveform (**c**) and the broadband storage (a prolonged delay of ~480 ns) and release of an RF pulse (**d**). **e**, Broadband digital-to-analogue gain on the RF arbitrary waveform via amplification of both the optical carrier and modulation sidebands followed by OE conversion. The full system response (EO S_{21}) surpasses the total digital electronic input power (−6 dBm, indicated by the 0 dB level), up to the 35 GHz modulation frequency, due to the 11.6 dB of optical gain and photodetector transimpedance gain (750 V W^{-1}) applied. **f**, Estimated generated RF power of triangular waves (depicted in the inset) as a function of the average optical power incident on the photodiode. The generated RF power in this case is based purely on the voltage induced by a photocurrent across a load of $R = 50\ \Omega$. The black line corresponds to a fitted photodiode conversion gain of ~19.4 V W^{-1}.

Discussion

In summary, we have presented a photonic-integrated EO-DiAL architecture that enables direct electrical-to-optical and digital-to-analogue conversion. We utilized this device to demonstrate two cases of practical use: as an efficient EO converter that is suitable for photonic computing accelerators, and as a novel microwave photonic arbitrary waveform generator. We leveraged a foundry-based process to demonstrate the scalable and consistent fabrication of compact TFLN circuits. The success of this process highlights the potential for microwave/optical-circuit co-design at the foundry level for synergistic photonic–electronic structures on the TFLN platform. Currently, our device features an average $V_{\pi}L \approx 3.05$ V cm, which is consistent with that expected from the foundry process specification. Segment S3 is still bandwidth-limited due to a trade-off between microwave loss and velocity matching. State-of-the-art EO modulators support EO 3 dB bandwidths that exceed 110 GHz (refs. 18,37) while simultaneously featuring a low V_{π}. These metrics are routinely achieved by the commercial foundry process today[38] due to further optimizations in the material stack and modulator architecture, including the folded design[39]. These advances would offer a smaller physical footprint of the EO-DiAL without sacrificing the bandwidth or V_{π} of its segments. Moreover, a much lower $V_{\pi}L$ is achievable at visible/near-infrared wavelengths while featuring bandwidths of tens of gigahertz[40,41]. Further improvements in modulator design and selection of the optical carrier frequency could substantially reduce the electrical energy consumption and facilitate photonic–electronic integration with high-speed complementary metal–oxide–semiconductor (CMOS) pulse pattern generators[5]. The optical energy consumption can also be reduced by optimizing propagation loss and fibre-to-chip coupling during the foundry process. For example, the insertion loss of our current device (4.65 dB per grating) can be reduced using bilayer taper edge coupling[42,43] combined with fibre array packaging, which are already foundry-compatible. The emerging photonic wirebonding technology[44,45], and packaging to suspended taper couplers[46,47], may offer additional solutions for the low-loss packaging of foundry-produced chips. Altogether, binary modulations with a voltage swing of tens of millivolts and lasers with an output of less than a milliwatt may be all that are needed for the encoding of analogue data in photonic computing applications, while achieving encoding fidelities that are comparable to those in this work. In RF-AWG applications, better EO efficiencies directly induce a greater slope efficiency and digital-to-analogue conversion gain (scaling inverse-quadratically with V_π)[36]. At the system level, a higher degree of integration using chip-scale lasers[48–52] and on-chip fast photodiodes[53] can lead to more compact systems and achieve similar performance improvements as previously described, due to enhanced lasing efficiencies[48,49], reduced coupling losses[51] and greater detector responsivities[53]. The hybrid and heterogeneous integration of gain material, distributed feedback laser sources and modified uni-travelling carrier photodiodes with TFLN circuits has already been successfully demonstrated[45,54–56], and it should be straightforward for such types of integration to be extended to the EO-DiAL. Finally, it is possible to increase the bit resolution further. Considering that modern commercial foundry capabilities include the sub-volt V_π, high-bandwidth TFLN amplitude modulator, longer segments can be incorporated to scale the bit resolution. A shorter segment may also be used, provided that the binary electrical driving amplitudes are also doubled, so that discretization of the relative phase remains consistent with our current demonstrations. Alternative architectures for scaling can involve combining two N-bit EO-DiALs in effective gain and loss configurations facilitated by an MZI to achieve $N+1$ bits, or simply by utilizing factor-of-two related binary electrical driving amplitudes and adding constant-length segments. However, we note that achieving an arbitrarily high bit resolution is not practically feasible due to the limited signal-to-noise ratio and the finite dynamic range of the EO conversion process. Importantly, it is also not necessary: the advantages of analogue photonic hardware are often realized in applications where a high bit precision is not critical (such as computing), and in many cases, limited precision can even enhance the performance without compromising the efficacy[8,12,31,57–59]. With the rapid proliferation of large language models (such as DeepSeek-V3[60]), there is growing interest in low-bit, quantized implementations motivated by the reduced electronic memory required to store model parameters as well as greater speed, energy efficiency and accuracy optimality[61]. These efforts are aligned with the four-bit EO-DiAL demonstration, where photonics may serve as specialized hardware to accelerate large-language-model-related inference tasks.

Given the speed and energy consumption assessments of the EO-DiAL, it may already be able to replace the essential EO modulator and electronic DAC in coherent photonic computing frameworks[62,63] based on large-scale TFLN EO circuits[55,56,64]. It is worth noting that multiple CW tones, such as from a potentially monolithic comb source[65–67], can simultaneously be used for parallelized data conversion across different wavelengths in a single pass of the device, which is common in photonic convolution acceleration leveraging the dispersive delay interleaving technique[68,69]. In terms of offering a competitive yet more manageable pathway for RF-AWG, the EO-DiAL may be combined with on-chip optical amplification[70–72] and tunable delays facilitated by microring all-pass filter arrays[73] to enhance the compactness of our preliminary demonstrations. Altogether, our results indicate that the continued development of novel analogue photonic hardware, such as the EO-DiAL, will broaden the design space for next-generation photonic computing, microwave photonic RF-AWG and other classical technologies such as high-capacity wireless/fibre-optic communications[74–77], light detection and ranging[78,79], microwave/mmWave photonic radar sensing[80,81] and signal processing[82,83]. Furthermore, we envision that such hardware will have an impact on nascent quantum technologies, for example, the optical and acoustic control of spin-based quantum memories using photonics-synthesized optical and microwave waveforms[84–86], and digital beamforming to probe arrays of artificial atoms[87,88].

Online content

Any methods, additional references, Nature Portfolio reporting summaries, source data, extended data, supplementary information, acknowledgements, peer review information; details of author contributions and competing interests; and statements of data and code availability are available at https://doi.org/10.1038/s41566-025-01719-9.

References

1. LeCun, Y., Bengio, Y. & Hinton, G. Deep learning. *Nature* **521**, 436–444 (2015).
2. Winzer, P. J., Neilson, D. T. & Chraplyvy, A. R. Fiber-optic transmission and networking: the previous 20 and the next 20 years. *Opt. Express* **26**, 24190–24239 (2018).
3. Graves, A. et al. Hybrid computing using a neural network with dynamic external memory. *Nature* **538**, 471–476 (2016).
4. Akopyan, F. et al. TrueNorth: design and tool flow of a 65 mW 1 million neuron programmable neurosynaptic chip. *IEEE Trans. Comput. Aided Des. Integr. Circuits Syst.* **34**, 1537–1557 (2015).
5. Chen, X. et al. All-electronic 100-GHz bandwidth digital-to-analog converter generating PAM signals up to 190 GBaud. *J. Lightwave Technol.* **35**, 411–417 (2017).
6. Song, H.-J. & Lee, N. Terahertz communications: challenges in the next decade. *IEEE Trans. Terahertz Sci. Technol.* **12**, 105–117 (2022).
7. Miller, D. A. B. Attojoule optoelectronics for low-energy information processing and communications. *J. Lightwave Technol.* **35**, 346–396 (2017).
8. Wetzstein, G. et al. Inference in artificial intelligence with deep optics and photonics. *Nature* **588**, 39–47 (2020).
9. Shastri, B. J. et al. Photonics for artificial intelligence and neuromorphic computing. *Nat. Photonics* **15**, 102–114 (2021).
10. Capmany, J. & Novak, D. Microwave photonics combines two worlds. *Nat. Photonics* **1**, 319–330 (2007).
11. Marpaung, D., Yao, J. & Capmany, J. Integrated microwave photonics. *Nat. Photonics* **13**, 80–90 (2019).
12. McMahon, P. L. The physics of optical computing. *Nat. Rev. Phys.* **5**, 717–734 (2023).
13. Marković, D., Mizrahi, A., Querlioz, D. & Grollier, J. Physics for neuromorphic computing. *Nat. Rev. Phys.* **2**, 499–510 (2020).
14. Rashidinejad, A., Li, Y. & Weiner, A. M. Recent advances in programmable photonic-assisted ultrabroadband radio-frequency arbitrary waveform generation. *IEEE J. Quantum Electron.* **52**, 1–17 (2016).
15. Bogaerts, W. et al. Programmable photonic circuits. *Nature* **586**, 207–216 (2020).
16. Shu, H. et al. Microcomb-driven silicon photonic systems. *Nature* **605**, 457–463 (2022).
17. Zhang, M., Wang, C., Kharel, P., Zhu, D. & Lončar, M. Integrated lithium niobate electro-optic modulators: when performance meets scalability. *Optica* **8**, 652–667 (2021).
18. Xu, M. et al. Dual-polarization thin-film lithium niobate in-phase quadrature modulators for terabit-per-second transmission. *Optica* **9**, 61–62 (2022).
19. Patel, D., Samani, A., Veerasubramanian, V., Ghosh, S. & Plant, D. V. Silicon photonic segmented modulator-based electro-optic DAC for 100 Gb/s PAM-4 generation. *IEEE Photonics Technol. Lett.* **27**, 2433–2436 (2015).
20. Dubé-Demers, R., LaRochelle, S. & Shi, W. Low-power DAC-less PAM-4 transmitter using a cascaded microring modulator. *Opt. Lett.* **41**, 5369–5372 (2016).

21. Simard, A. D., Filion, B., Patel, D., Plant, D. & LaRochelle, S. Segmented silicon MZM for PAM-8 transmissions at 114 Gb/s with binary signaling. *Opt. Express* **24**, 19467–19472 (2016).
22. Huynh, T. N. et al. Flexible transmitter employing silicon-segmented Mach–Zehnder modulator with 32-nm CMOS distributed driver. *J. Lightwave Technol.* **34**, 5129–5136 (2016).
23. Samani, A. et al. Experimental parametric study of 128 Gb/s PAM-4 transmission system using a multi-electrode silicon photonic Mach Zehnder modulator. *Opt. Express* **25**, 13252–13262 (2017).
24. Sobu, Y. et al. High-speed optical digital-to-analog converter operation of compact two-segment all-silicon Mach–Zehnder modulator. *J. Lightwave Technol.* **39**, 1148–1154 (2021).
25. Jafari, O., Zhalehpour, S., Shi, W. & LaRochelle, S. DAC-less PAM-4 slow-light silicon photonic modulator providing high efficiency and stability. *J. Lightwave Technol.* **39**, 5074–5082 (2021).
26. Wang, C. et al. Integrated lithium niobate electro-optic modulators operating at CMOS-compatible voltages. *Nature* **562**, 101–104 (2018).
27. Hu, Y. et al. On-chip electro-optic frequency shifters and beam splitters. *Nature* **599**, 587–593 (2021).
28. Hu, Y. et al. Integrated electro-optics on thin-film lithium niobate. *Nat. Rev. Phys.* **7**, 237–254 (2025).
29. Zhang, M., Wang, C., Cheng, R., Shams-Ansari, A. & Lončar, M. Monolithic ultra-high-*Q* lithium niobate microring resonator. *Optica* **4**, 1536–1537 (2017).
30. Zhu, X. et al. Twenty-nine million intrinsic *Q*-factor monolithic microresonators on thin-film lithium niobate. *Photonics Res.* **12**, A63–A68 (2024).
31. Zhou, H. et al. Photonic matrix multiplication lights up photonic accelerator and beyond. *Light Sci. Appl.* **11**, 30 (2022).
32. Cundiff, S. T. & Weiner, A. M. Optical arbitrary waveform generation. *Nat. Photonics* **4**, 760–766 (2010).
33. Wang, J. et al. Reconfigurable radio-frequency arbitrary waveforms synthesized in a silicon photonic chip. *Nat. Commun.* **6**, 5957 (2015).
34. Tan, M. et al. Photonic RF arbitrary waveform generator based on a soliton crystal micro-comb source. *J. Lightwave Technol.* **38**, 6221–6226 (2020).
35. Fischer, B. et al. Autonomous on-chip interferometry for reconfigurable optical waveform generation. *Optica* **8**, 1268–1276 (2021).
36. Cox, C. H., Ackerman, E. I., Betts, G. E. & Prince, J. L. Limits on the performance of RF-over-fiber links and their impact on device design. *IEEE Trans. Microw. Theory Tech.* **54**, 906–920 (2006).
37. Kharel, P., Reimer, C., Luke, K., He, L. & Zhang, M. Breaking voltage–bandwidth limits in integrated lithium niobate modulators using micro-structured electrodes. *Optica* **8**, 357–363 (2021).
38. St-Arnault, C. et al. Net 3.2 Tbps 225 Gbaud PAM4 O-band IM/DD 2 km transmission using FR8 and DR8 with a CMOS 3 nm SerDes and TFLN modulators. Preprint at https://arxiv.org/abs/2503.24147 (2025).
39. Della Torre, A. et al. Folded electro-optical modulators operating at CMOS voltage level in a thin-film lithium niobate foundry process. *Opt. Express* **33**, 6747–6757 (2025).
40. Xue, S. et al. Full-spectrum visible electro-optic modulator. *Optica* **10**, 125–126 (2023).
41. Renaud, D. et al. Sub-1 Volt and high-bandwidth visible to near-infrared electro-optic modulators. *Nat. Commun.* **14**, 1496 (2023).
42. He, L. et al. Low-loss fiber-to-chip interface for lithium niobate photonic integrated circuits. *Opt. Lett.* **44**, 2314–2317 (2019).
43. Liu, X. et al. Ultra-broadband and low-loss edge coupler for highly efficient second harmonic generation in thin-film lithium niobate. *Adv. Photonics Nexus* **1**, 016001 (2022).
44. Cheng, R. et al. Single-drive electro-optic frequency comb source on a photonic-wire-bonded thin-film lithium niobate platform. *Opt. Lett.* **49**, 3504–3507 (2024).
45. Franken, C. A. A. et al. High-power and narrow-linewidth laser on thin-film lithium niobate enabled by photonic wire bonding. *APL Photonics* **10**, 026107 (2025).
46. Zeng, B. et al. Cryogenic packaging of nanophotonic devices with a low coupling loss <1 dB. *Appl. Phys. Lett.* **123**, 161106 (2023).
47. Assumpcao, D. et al. A thin film lithium niobate near-infrared platform for multiplexing quantum nodes. *Nat. Commun.* **15**, 10459 (2024).
48. Botez, D., Garrod, T. & Mawst, L. J. High CW wallplug efficiency 1.5 micron-emitting diode lasers. In *2015 IEEE Photonics Conference (IPC)* 551–552 (IEEE, 2015); https://doi.org/10.1109/IPCon.2015.7323726
49. Mashanovitch, M. et al. High-power, efficient DFB laser technology for RF photonics links. In *2018 IEEE Avionics and Vehicle Fiber-Optics and Photonics Conference (AVFOP)* 1–2 (IEEE, 2018); https://doi.org/10.1109/AVFOP.2018.8550469
50. Jin, W. et al. Hertz-linewidth semiconductor lasers using CMOS-ready ultra-high-*Q* microresonators. *Nat. Photonics* **15**, 346–353 (2021).
51. Yu, M. et al. Integrated electro-optic isolator on thin-film lithium niobate. *Nat. Photonics* **17**, 666–671 (2023).
52. Xiang, C. et al. 3D integration enables ultralow-noise isolator-free lasers in silicon photonics. *Nature* **620**, 78–85 (2023).
53. Guo, X. et al. High-performance modified uni-traveling carrier photodiode integrated on a thin-film lithium niobate platform. *Photonics Res.* **10**, 1338–1343 (2022).
54. Shams-Ansari, A. et al. Electrically pumped laser transmitter integrated on thin-film lithium niobate. *Optica* **9**, 408–411 (2022).
55. Lin, Z. et al. 120 GOPS Photonic tensor core in thin-film lithium niobate for inference and in situ training. *Nat. Commun.* **15**, 9081 (2024).
56. Hu, Y. et al. Integrated lithium niobate photonic computing circuit based on efficient and high-speed electro-optic conversion. Preprint at https://arxiv.org/abs/2411.02734 (2024)
57. Nahmias, M. A. et al. Photonic multiply-accumulate operations for neural networks. *IEEE J. Sel. Top. Quantum Electron.* **26**, 1–18 (2020).
58. Shen, Y. et al. Deep learning with coherent nanophotonic circuits. *Nat. Photonics* **11**, 441–446 (2017).
59. Gupta, S., Agrawal, A., Gopalakrishnan, K. & Narayanan, P. Deep learning with limited numerical precision. In *Proc. 32nd International Conference on Machine Learning* Vol. 37 (eds Bach, F. & Blei, D.) 1737–1746 (PMLR, 2015).
60. DeepSeek-AI et al. DeepSeek-V3 technical report. Preprint at https://arxiv.org/abs/2412.19437 (2025).
61. Dettmers, T. & Zettlemoyer, L. The case for 4-bit precision: k-bit inference scaling laws. In *Proc. 40th International Conference on Machine Learning* Vol. 202 (eds Krause, A. et al.) 7750–7774 (PMLR, 2023).
62. Hamerly, R., Bernstein, L., Sludds, A., Soljačić, M. & Englund, D. Large-scale optical neural networks based on photoelectric multiplication. *Phys. Rev. X* **9**, 021032 (2019).
63. Chen, Z. et al. Deep learning with coherent VCSEL neural networks. *Nat. Photonics* **17**, 723–730 (2023).
64. Ou, S. et al. Hypermultiplexed integrated photonics-based optical tensor processor. *Sci. Adv.* **11**, eadu0228 (2025).
65. Hu, Y. et al. High-efficiency and broadband on-chip electro-optic frequency comb generators. *Nat. Photonics* **16**, 679–685 (2022).
66. Song, Y., Hu, Y., Zhu, X., Yang, K. & Lončar, M. Octave-spanning Kerr soliton frequency combs in dispersion- and dissipation-engineered lithium niobate microresonators. *Light Sci. Appl.* **13**, 225 (2024).

67. Song, Y., Zhu, X., Zuo, X., Huang, G. & Lončar, M. Stable gigahertz- and mmWave-repetition-rate soliton microcombs on X-cut lithium niobate. *Optica* **12**, 693–701 (2025).
68. Xu, X. et al. 11 TOPS photonic convolutional accelerator for optical neural networks. *Nature* **589**, 44–51 (2021).
69. Bai, B. et al. Microcomb-based integrated photonic processing unit. *Nat. Commun.* **14**, 66 (2023).
70. Chen, Z. et al. Efficient erbium-doped thin-film lithium niobate waveguide amplifiers. *Opt. Lett.* **46**, 1161–1164 (2021).
71. Zhou, J. et al. On-chip integrated waveguide amplifiers on erbium-doped thin-film lithium niobate on insulator. *Laser Photon. Rev.* **15**, 2100030 (2021).
72. Jia, Y. et al. Integrated photonics based on rare-earth ion-doped thin-film lithium niobate. *Laser Photon. Rev.* **16**, 2200059 (2022).
73. Cardenas, J. et al. Wide-bandwidth continuously tunable optical delay line using silicon microring resonators. *Opt. Express* **18**, 26525–26534 (2010).
74. Koenig, S. et al. Wireless sub-THz communication system with high data rate. *Nat. Photonics* **7**, 977–981 (2013).
75. Pfeifle, J. et al. Coherent terabit communications with microresonator Kerr frequency combs. *Nat. Photonics* **8**, 375–380 (2014).
76. Marin-Palomo, P. et al. Microresonator-based solitons for massively parallel coherent optical communications. *Nature* **546**, 274–279 (2017).
77. Rizzo, A. et al. Massively scalable Kerr comb-driven silicon photonic link. *Nat. Photonics* **17**, 781–790 (2023).
78. Siddharth, A. et al. Ultrafast tunable photonic-integrated extended-DBR Pockels laser. *Nat. Photonics* **19**, 709–717 (2025).
79. Xue, S. et al. Pockels laser directly driving ultrafast optical metrology. *Light Sci. Appl.* **14**, 209 (2025).
80. Ghelfi, P. et al. A fully photonics-based coherent radar system. *Nature* **507**, 341–345 (2014).
81. Zhu, S. et al. Integrated lithium niobate photonic millimetre-wave radar. *Nat. Photonics* **19**, 204–211 (2025).
82. Liu, W. et al. A fully reconfigurable photonic integrated signal processor. *Nat. Photonics* **10**, 190–195 (2016).
83. Feng, H. et al. Integrated lithium niobate microwave photonic processing engine. *Nature* **627**, 80–87 (2024).
84. Maity, S. et al. Coherent acoustic control of a single silicon vacancy spin in diamond. *Nat. Commun.* **11**, 193 (2020).
85. Riedel, D. et al. Efficient photonic integration of diamond color centers and thin-film lithium niobate. *ACS Photonics* **10**, 4236–4243 (2023).
86. Knaut, C. M. et al. Entanglement of nanophotonic quantum memory nodes in a telecom network. *Nature* **629**, 573–578 (2024).
87. Menssen, A. J. et al. Scalable photonic integrated circuits for high-fidelity light control. *Optica* **10**, 1366–1372 (2023).
88. Christen, I. et al. An integrated photonic engine for programmable atomic control. *Nat. Commun.* **16**, 82 (2025).

Yunxiang Song[1,2,9] ✉, Yaowen Hu[1,3,9] ✉, Xinrui Zhu[1], Keith Powell[1], Letícia Magalhães[1], Fan Ye[4], Hana K. Warner[1], Shengyuan Lu[1], Xudong Li[1], Dylan Renaud[1,4], Norman Lippok[1,5], Di Zhu[6,7,8], Benjamin Vakoc[5], Mian Zhang[4], Neil Sinclair[1] & Marko Lončar[1] ✉

[1]John A. Paulson School of Engineering and Applied Sciences, Harvard University, Cambridge, MA, USA. [2]Quantum Science and Engineering, Harvard University, Cambridge, MA, USA. [3]State Key Laboratory for Mesoscopic Physics and Frontiers Science Center for Nano-optoelectronics, School of Physics, Peking University, Beijing, China. [4]HyperLight Corporation, Cambridge, MA, USA. [5]Wellman Center of Photomedicine, Harvard Medical School and Massachusetts General Hospital, Boston, MA, USA. [6]Department of Materials Science and Engineering, National University of Singapore, Singapore, Singapore. [7]Centre for Quantum Technologies, National University of Singapore, Singapore, Singapore. [8]A*STAR Quantum Innovation Centre (Q.InC), Institute of Materials Research and Engineering (IMRE), Agency for Science, Technology and Research (A*STAR), Singapore, Singapore. [9]These authors contributed equally: Yunxiang Song, Yaowen Hu. ✉e-mail: ysong1@g.harvard.edu; yaowenhu@pku.edu.cn; loncar@seas.harvard.edu

Data availability

All data needed to evaluate the conclusions of the paper are available within the Article and its Supplementary Information.

Acknowledgements

We thank K. Richard, N. Hoffman, M. Roberts and Keysight Technologies, Inc. for technological support, J. Jacobson for assistance and D. Plant and G. Hills for discussions. This work is supported by the Korea Advanced Institute of Science and Technology, grant number NRF-2022M3K4A1094782 (to Y.S., Y.H. and X.L.), the Defense Advanced Research Projects Agency, grant number HR001120C0137 (to Y.H. and L.M.), the National Science Foundation (NSF), grant numbers OMA-2137723 (to Y.H.), NSF 2138068 (to Y.H.) and NSF EEC-1941583 (to K.P., H.K.W. and N.S.), the Department of the Navy, grant number N6833522C0413 (to X.Z. and K.P.), Amazon Web Services (AWS), grant number A50791 (to K.P., L.M. and D.R.), DRS Daylight Solutions, Inc., award A56097 (to L.M.), NASA grant number 80NSSC22K0262 (to N.S.), the National Institutes of Health, grant numbers NIH P41EB015903 (to N.L. and B.V.) and NIH R21EY031895 (to N.L. and B.V.) and the Singapore National Research Foundation grant numbers NRF2022-QEP2-01-P07 and NRF-NRFF15-2023-0005 (to D.Z.). Y.S. acknowledges support from the AWS Generation Q Fund at the Harvard Quantum Initiative. L.M. acknowledges support from the Capes-Fulbright and Behring Foundation fellowships. H.K.W. acknowledges support from the National Science Foundation Graduate Research Fellowship Program. S.L. acknowledges support from the A*STAR National Science Scholarship. The views, opinions and/or findings expressed are those of the authors and should not be interpreted as representing the official views or policies of the Department of Defense or the US Government.

Author contributions

M.L. and Y.H. conceived the project. Y.S. and Y.H. designed the experiments. Y.S. performed the measurements and analysed the data with Y.H. assisting. Y.H. led the foundry tapeout with F.Y. assisting. X.Z., Y.S. and Y.H. fabricated the early versions of the device. K.P., L.M., H.K.W., S.L., X.L., D.R., N.L., D.Z., B.V., M.Z. and N.S. helped with the project. Y.S., Y.H. and M.L. wrote the manuscript with contributions from all authors. M.L. supervised the project.

Competing interests

F.Y., D.R., M.Z. and M.L. are involved in developing lithium niobate technologies at HyperLight Corporation. The remaining authors declare no competing interests.

Additional information

Supplementary information The online version contains supplementary material available at https://doi.org/10.1038/s41566-025-01719-9.

Correspondence and requests for materials should be addressed to Yunxiang Song, Yaowen Hu or Marko Lončar.

Peer review information *Nature Photonics* thanks Jose Capmany, Charles Roques-Carmes and the other, anonymous, reviewer(s) for their contribution to the peer review of this work.